Available online at www.sciencedirect.com
ScienceDirect
International Journal of Heat and Mass Transfer 51 (2008) 4055–4068
International Journal of HEAT and MASS TRANSFER
www.elsevier.com/locate/ijhmt

A numerical investigation on the fluid flow and heat transfer in the confined impinging slot jet in the low Reynolds number region for different channel heights

H.G. Lee [a], H.S. Yoon [b], M.Y. Ha [a,*]

[a] School of Mechanical Engineering, Pusan National University, San 30, Jangjeon-Dong, Kumjung Gu, Busan 609-735, Republic of Korea
[b] Advanced Ship Engineering Research Center, Pusan National University, San 30, Jangjeon-Dong, Kumjung Gu, Busan 609-735, Republic of Korea

Received 7 March 2007; received in revised form 8 January 2008
Available online 17 March 2008

Abstract

The numerical solution is obtained for unsteady two-dimensional fluid flow and heat transfer in a confined impinging slot jet using the finite volume method. In order to consider the effect of Reynolds number and height ratio on the flow and temperature fields in the channel, the numerical simulations were performed for different Reynolds numbers of 50–500 and different height ratios of 2–5. The critical Reynolds number, beyond which the flow and thermal fields change their state from steady to unsteady, depends on the Reynolds number and height ratio. The unsteadiness gives a big impact on the flow and temperature fields and as a result the pressure coefficient, skin friction coefficient and Nusselt number in the unsteady region show different characteristics from those in the steady region.

1. Introduction

Impinging jets are jets of fluid on an impingement surface that needs to be cooled/heated or dried. These impinging jets are widely applied in many industrial and engineering applications such as rapid cooling/heating processes, drying of papers, films and foods, freezing of tissue, coating and tempering of glass and metal, because of their high heat and mass transfer rates and high efficiency. The advantage of impinging jet flow is its ease to adjust the location of interest and to remove a large amount of heat (or mass) on the impinging surface due to the thin hydrodynamic and thermal (or concentration) boundary layers around the stagnation region. In recent years, the power dissipation from electrical components becomes larger because of their high density. The impinging jet is used as a promising candidate to remove more heat from electrical components. However, in electronic packaging, because space and size are limited, it is difficult to properly implement the impinging jet which works at a low Reynolds number under the low operating pressure condition.

There have been many experimental and numerical studies to investigate the flow structures and heat transfer mechanisms in detail to obtain the optimal operating conditions of impinging jets for different industrial and engineering applications. Most of these previous studies are concerned with high Reynolds number jets because of industrial applications. Then, only several research papers are available on low Reynolds number jets. Sparrow and Wong [1] derived the mass transfer correlation for the impinging slot jet flows at a Reynolds number of $150 < Re < 950$ using the naphthalene sublimation technique and the analogy of heat and mass transfer. Chen et al. [2] carried out an experimental and numerical study to investigate the high Schmidt-number mass transfer to a line electrode in laminar impinging slot jet flows for the slot-based Reynolds number from 220 to 690. Their experimental and theoretical results show that the peak values in mass transfer occur at a point one-half to one jet width away from the stagnation point, which

* Corresponding author. Tel.: +82 51 510 2440; fax: +82 51 515 3101.
E-mail address: myha@pusan.ac.kr (M.Y. Ha).

0017-9310/$ - see front matter © 2008 Elsevier Ltd. All rights reserved.
doi:10.1016/j.ijheatmasstransfer.2008.01.015

Nomenclature

C_f	friction coefficient
C_P	pressure coefficient
D	jet nozzle width
H	nozzle-to-plate spacing
L	channel length
Nu	local Nusselt number
p	dimensionless pressure
Pr	Prandtl number
Re	Reynolds number ($=v_{jet}D/v$)
Re_c	critical Reynolds number
t	dimensionless time
t_p	period of time integration
T	dimensionless temperature
u, v	dimensionless velocity in x and y direction
x, y	cartesian coordinates

Greek symbols

α	thermal diffusivity
ρ	density
v	kinematic viscosity

Sub/superscripts

c	critical value
jet	nozzle exit jet
ref	reference value
RMS	root mean square
stag	stagnation point
w	bottom wall
*	dimensional value
–	time-averaged quantity
$\langle\ \rangle$	surface-averaged quantity

was not observed by the earlier studies. Aldabbagh and Sezai [3] investigated the flow and heat transfer characteristics of impinging laminar multiple square jets through the solution of the three-dimensional Navier–Stokes and energy equations in steady state for different jet-to-jet spacings and nozzle exit to plate distances. Chiriac and Ortega [4] computed the steady and unsteady flow and heat transfer due to a confined two-dimensional slot jet impinging on an isothermal plate using a numerical finite-difference approach for different Reynolds numbers based on hydraulic diameters in the range of 250-750 at the fixed Prandtl number of 0.7 and jet-to-plate spacing of 5. The flow and heat transfer at the Reynolds numbers of 250 and 350 were steady whereas those at the Reynolds number of 750 was unsteady and showed a very complex pattern with buckling, flapping and sweeping of the jet due to vortex shedding and a non-linear interaction between the jet and the channel fluid. The stagnation Nusselt number is directly proportional to the jet Reynolds number at the steady state condition, whereas those at the unsteady condition are less dependent on the Reynolds number. Lee et al.[5] numerically investigates two-dimensional laminar slot jet phenomena in the presence of an applied magnetic field to control vortices and enhance heat transfer. The visualization and measurement of heat transfer characteristics were conducted by Hsieh et al. [6] for the jet Reynolds number varying from 0 to 1623. They noted that vortex flow at even higher Reynolds numbers becomes unstable due to the inertia driven flow instability. Phares et al. [7] presented a method for the theoretical determination of the wall shear stress under impinging jets for a wide range of Reynolds numbers and jet heights. They compared their theoretically predicted results with available wall shear stress measurements. They found that the electrochemical method in submerged impinging liquid jets could predict the wall shear stress in the impingement region most accurately among any of the indirect methods and determine an empirical relation describing the rise in wall shear stress due to compressibility effects in high-velocity impinging jets. Chung et al. [8] performed direct numerical simulations of an unsteady impinging jet to study momentum and heat transfer characteristics by solving the unsteady compressible Navier–Stokes equations using a high-order finite-difference method with non-reflecting boundary conditions. They investigated the effect of primary and secondary vortices on the local heat transfer and fluid flow. Law and Masliyah [9] numerically studied impinging jet flow with Reynolds numbers between 100 and 400, and jet-to-plate spacings between 2 and 4. The detailed flow characteristics are considered in steady state without any heat transfer. Schafer et al. [10] calculated the effects of the jet velocity profile and pertinent dimensionless parameters on flow and heat transfer conditions. For the different jet velocity profiles, uniform and fully developed profiles, heat transfer and flow field were compared. Miyazaki and Silberman [11] analyzed theoretically the two-dimensional laminar jet impinging on a flat plate. They evaluated the local friction factor and Nusselt numbers. Sahoo and Sharif [12] investigated the associate heat transfer process in a mixed convection regime for a range of Reynolds numbers (100–500) and Richardson numbers (0–10). Chou and Hung [13] numerically studied and suggested new correlations of Nusselt numbers in terms of Re and H/D at the stagnation line for three different jet exit velocity profiles (uniform, Gaussian and parabolic). Chatterjee and Deviprasath [14] presented the role of upstream vorticity diffusion for off-stagnation point Nusselt number maxima in laminar impinging jets at small height ratios. Lin et al. [15] performed experiment which includes the parametric study of jet Reynolds number and jet separation distance on heat transfer characteristics of the heated target surface. They classified an impinging jet flow into laminar or turbulent according to the turbulent intensity.

van Heiningen et al. [16] investigated numerically the effects of uniform suction and nozzle exit velocity profile on the flow and heat transfer characteristics of a semi-confined laminar impinging slot jet. They reported that two different nozzle exit velocity profiles, uniform and parabolic, affected the heat transfer and flow characteristics significantly.

In the present study, we investigated the dependency of flow and thermal fields of the confined impinging jet on the Reynolds number and height ratio. We obtained the numerical solutions for unsteady two-dimensional governing equations for fluid flow and heat transfer using the finite volume method. We calculated the instantaneous and time-averaged streamlines, time- and surface-averaged friction coefficients, time-averaged pressure coefficients and Nusselt numbers at the stagnation point as a function of the Reynolds number for different height ratios. Hence, the results obtained for the wide range of low Reynolds number can identify the transitions to the unsteady regime and their effects on the characteristics of flow and heat transfer.

2. Governing equations

Fig. 1 shows the computational domain and coordinate system for the two-dimensional confined impinging jet considered in the present study. The unsteady two-dimensional dimensionless continuity, Navier–Stokes and energy equations that were solved are defined as

$$\nabla \cdot \vec{u} = 0 \tag{1}$$

$$\frac{\partial \vec{u}}{\partial t} + \vec{u} \cdot \nabla \vec{u} = -\nabla p + \frac{1}{Re} \nabla^2 \vec{u} \tag{2}$$

$$\frac{\partial T}{\partial t} + \vec{u} \cdot \nabla T = \frac{1}{Re \cdot Pr} \nabla^2 T \tag{3}$$

The dimensionless variables in the above equations are defined as

$$t = \frac{v_{\text{jet}} t^*}{D}, \quad \vec{u} = \frac{\vec{u}^*}{v_{\text{jet}}}, \quad p = \frac{p^*}{\rho v_{\text{jet}}^2}, \quad T = \frac{T^* - T_{\text{w}}}{T_{\text{jet}} - T_{\text{w}}} \tag{4}$$

In the above equations, ρ, v_{jet}, T_{jet}, T_{w}, and D represent the density, inlet jet velocity, inlet jet temperature, bottom wall temperature and jet width, respectively. The superscript * in Eq. (4) represents the dimensional variables. $t, \vec{u}, p$ and T are the non-dimensional time, velocity vector, pressure and temperature. The above non-dimensionalization results in two dimensionless parameters: $Re = v_{\text{jet}} D/\nu$ and $Pr = \nu/\alpha$ where ν and α are the kinematic viscosity and thermal diffusivity. In the simulations to be reported here the Prandtl number, Pr, has been taken to be 0.7. We limit attention to the case of incompressible flow with constant thermodynamic and transport properties for the fluid. We also assume that the flow is two-dimensional and invariant along the spanwise direction for the low Reynolds numbers considered in the present problem.

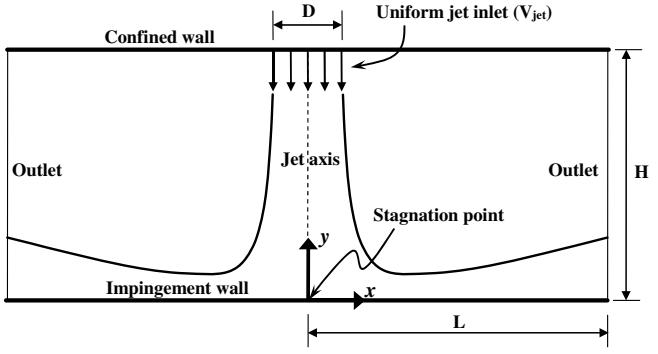

Fig. 1. Computational domain and coordinate system for a two-dimensional confined impinging jet.

3. Numerical methodology

The central difference scheme with second-order accuracy based on the finite volume method is used for the spatial discretization [17]. A two-step time-split scheme is used to advance the flow field. First the velocity is advanced from time level 'n' to an intermediate level by solving the advection–diffusion equation. In the advection–diffusion step, the nonlinear terms are treated explicitly using the second-order Adams–Bashforth scheme. The diffusion terms are treated implicitly using the Crank–Nicolson scheme. Then a Poisson equation for pressure is solved fully implicitly. The final divergence-free velocity field at '$n+1$' is obtained with a pressure-correction step. The temperature field is advanced in a similar manner with the second-order Adams–Bashforth scheme for the advection term and the Crank–Nicolson scheme for the diffusion term [18].

Once the velocity and temperature fields are obtained, the local, time- and/or surface-averaged pressure coefficients, friction coefficients and Nusselt numbers are defined as

$$\begin{aligned} C_{\text{p}} &= \frac{p - p_{\text{jet}}}{1/2 \rho v_{\text{jet}}^2}, \quad \overline{C_{\text{p}}} = \frac{1}{t_p} \int_{t_1}^{t_2} C_{\text{p}} \mathrm{d}t \\ C_{\text{f}} &= \frac{\tau_{\text{w}}}{1/2 \rho v_{\text{jet}}^2}, \quad \langle \overline{C_{\text{f}}} \rangle = \frac{1}{t_{\text{p}}} \frac{1}{L} \int_{t_1}^{t_2} \int_{-L/2}^{L/2} C_{\text{f}} \mathrm{d}x \mathrm{d}t \\ Nu &= \left. \frac{\partial T}{\partial y} \right|_{\text{wall}}, \quad \overline{Nu} = \frac{1}{t_{\text{p}}} \int_{t_1}^{t_2} Nu \mathrm{d}t \end{aligned} \tag{5}$$

where, τ_{w} is wall shear stress and $t_{\text{p}} (= t_2 - t_1)$ is the period of time integration.

The boundary conditions used in the present study are defined as

$$\begin{aligned} &\text{Inlet} : u = 0,\ v = -1,\ T = 1 \\ &\text{Upper wall} : u = v = 0,\ \partial T/\partial y = 0 \\ &\text{Lower wall} : u = 0,\ v = 0,\ T = 0 \\ &\text{Lateral exit} : \frac{\partial u}{\partial t} + C \frac{\partial u}{\partial x} = 0,\ \frac{\partial v}{\partial t} + C \frac{\partial v}{\partial x} = 0,\ \frac{\partial T}{\partial t} + C \frac{\partial T}{\partial x} = 0 \end{aligned}$$

At the lateral exit regions, a convective boundary condition based on the hyperbolic equation is used to prevent any

flow reflection or distortion at the outlet [19,20]. This convective outlet boundary condition also reduces the CPU time, the upstream influence of the outlet and the necessary downstream extent of the domain. The convective velocity C represents a mean value of stream-wise direction velocities at the exit.

Fig. 2 shows the grid distribution and the number of domains used in the present study. The number of grid points used in the present calculation is 1001×101 ($x \times y$) and the number of domains used is 10. The condition of CFL < 0.3 is chosen to determine the non-dimensional time step used in the present calculations and as a result a time step of 0.005 is used for all the calculations. The computations are advanced in time until it is observed that the pressure and heat transfer coefficients have reached a statistically stationary state. The developed computer code is parallelized based on the MPI (Message Passing Interface) to increase the computational speed [21]. The number of processors used is 5 in the x-direction and 2 in the y-direction, respectively, as shown in Fig. 2. The same number of grid points is allocated to each processor.

In advance, the grid independence study to find optimum grid resolution has been performed for $H/D = 5$ at $Re = 500$ and $L = 30$. The grid dimensions of the coarse, medium and fine grid systems considered are 601×75, 1001×101 and 1501×125 ($x \times y$), respectively. The time-averaged pressure coefficients and Nusselt numbers at the stagnation point ($\overline{C}_{p,stag}, \overline{Nu}_{stag}$) for the medium and fine grid systems are very close. However, these values of coarse grid system show the little deviation from those of the medium and fine grid systems as shown in Table 1. Accordingly, we used the medium grid system of 1001×101 ($x \times y$) in the present study. Also, the computational domain size has been tested for $L = 10$, 20, 30 and 40 for the case of $H/D = 5$ at $Re = 150$ and 500, using the grid system of 601×101, 801×101, 1001×101 and 1201×101 respectively. Table 2 shows the results for the domain size dependency test case study. Then, the domain size $L = 30$ was chosen for the appropriate domain size based on efficient numerical calculations.

Table 1
Test cases and results of grid independence study

Case	N_x	N_y	$\overline{C}_{p,stag}$	$\overline{Nu}_{stag}$
1	601	75	0.827	8.626
2	1001	101	0.786	8.085
3	1501	125	0.779	7.961

Table 2
Test cases and results of computational domain size independence study

Case	Re	L	$\overline{C}_{p,stag}$	$\overline{Nu}_{stag}$
1	150	10	0.957	5.527
2	150	20	0.957	5.528
3	150	30	0.957	5.528
4	150	40	0.957	5.528
5	500	10	0.783	8.081
6	500	20	0.785	8.067
7	500	30	0.787	8.061
8	500	40	0.786	8.058

To validate the present computational method, the fluid flow and heat transfer for the confined impinging jet was conducted when $H/D = 5$ at $Re = 125$ and 250. Fig. 3 shows that the present results of time-averaged pressure coefficients and Nusselt numbers along the lower (impingement) wall are in good agreement with those of previous researches [4,5].

4. Results and discussion

Figs. 4 and 5 show the time-histories of pressure coefficients at the stagnation point ($C_{P,stag}$) and their corresponding root-mean-square (RMS) value ($RMS_{Cp,stag}$) for different Reynolds numbers and height ratios. In the present study, we defined the critical Reynolds number as a Reynolds number beyond which the flow starts to change its state from steady to unsteady. Within the range of Reynolds numbers considered in this study with the interval of 50, the critical Reynolds numbers ($Re_{C,2}$, $Re_{C,3}$, $Re_{C,4}$ and $Re_{C,5}$) for the different H/Ds of 2, 3, 4 and 5 are identified

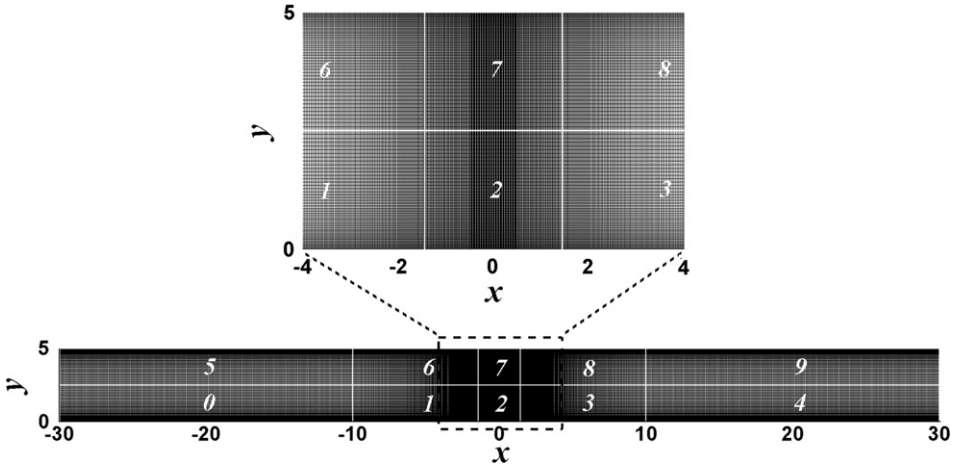

Fig. 2. Grid distribution and the number of domain used ($H/D = 5$).

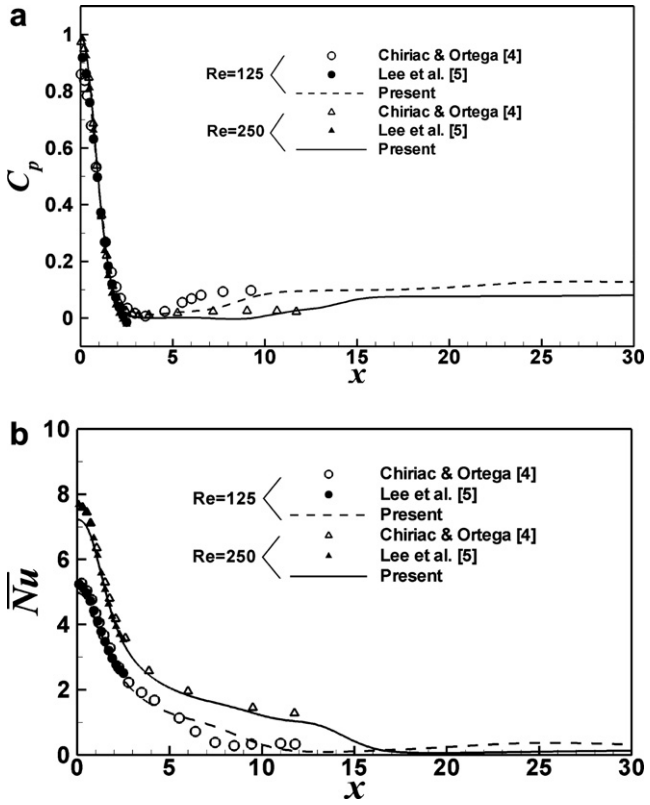

Fig. 3. Time-averaged quantities along the impingement wall at $H/D = 5$; (a) pressure coefficient and (b) Nusselt number.

by observing the time-histories of pressure coefficients ($C_{P,stag}$) and their RMS value at the stagnation point for different Reynolds numbers and height ratios.

The critical Reynolds numbers for $H/D = 2, 3, 4$ and 5 are $Re_{C,2} = 350$, $Re_{C,3} = 300$, $Re_{C,4} = 300$ and $Re_{C,5} = 250$, respectively. The critical Reynolds number decreases with increasing height ratio, meaning that the flow and temperature fields change their state from steady to unsteady at the smaller Reynolds number due to increasing unsteadiness with increasing H/D.

When the Reynolds number is less than the critical Reynolds number, the flow and temperature fields are steady and as a result $C_{P,stag}$ is constant and the RMS of $C_{P,stag}$ is zero, as shown in Figs. 4 and 5. If the Reynolds number is larger than the critical Reynolds number, the flow and temperature fields are time-dependent and $C_{P,\,stag}$ oscillates with a positive RMS value of $C_{P,stag}$. Under the unsteady condition where the Reynolds number is greater than the critical Reynolds number, the oscillating amplitude of $C_{P,stag}$ and the corresponding RMS of $C_{P,stag}$ increases significantly with increasing Reynolds number and height ratio, meaning that the unsteadiness increases with increasing Reynolds number and height ratio.

For the case of $H/D = 2$, $C_{P,stag}$ is independent of time in the range of $Re \leqslant Re_{C,2} = 350$. When $Re > 350$, $RMS_{Cp,stag}$ is larger than 0 and $C_{P,stag}$ starts to oscillate with a small oscillating amplitude, as shown in Figs. 4a and 5.

For the cases of $H/D = 3$ and 4, the critical Reynolds number is 300. When $Re > 300$ at $H/D = 3$ and 4, $C_{P,stag}$ shows time-dependent behavior as shown in Fig. 4b and c, and the RMS of $C_{P,stag}$ increases with increasing Reynolds number as shown in Fig. 5. As H/D increases, the oscillating amplitude of $C_{P,stag}$ increases with increasing unsteadiness and the RMS of $C_{P,stag}$ for $H/D = 3$ and 4 is larger than that for $H/D = 2$. As a result the critical Reynolds number for $H/D = 3$ and 4 is less than that for $H/D = 2$, meaning that the flow changes its state from steady to unsteady at the lower Reynolds number as H/D increases.

For the case of $H/D = 5$, the critical Reynolds number is 250, which is less than that for the cases of $H/D = 2$, 3 and 4. When the flow and temperature fields are time-dependent, the oscillating amplitude and the RMS of $C_{P,stag}$ for $H/D = 5$ are much larger than those for $H/D = 2$, 3 and 4.

Figs. 6–9 show the instantaneous streamlines for different Reynolds numbers of 50–500 and different height ratios of 2–5 to show the unsteady flow characteristics after they reach the fully developed state.

When $H/D = 2$ at $Re = 50$, the flow is steady and has a symmetric shape about the jet axis ($x = 0$). Two symmetric main re-circulating vortices are formed near the jet inlet due to the jet entrainment. When $Re = 150$ at $H/D = 2$, the two main re-circulating vortices elongate along the direction of jet exit and their size becomes bigger than that at $Re = 50$, due to the increasing convective force with increasing Reynolds number. The stronger convective motion contributes to the flow separation and the formation of secondary vortices on the lower wall as shown in Fig. 6b. As we increase the Reynolds number to 300, the pair of symmetric vortices still elongate and the secondary vortices on the lower wall move further outward to the lateral exit. Because the value of $RMS_{Cp,stag}$ is very small when $Re = 400$ as shown in Fig. 5, the unsteadiness of the flow at $Re = 400$ is very weak and as a result the flow at $Re = 400$ is similar to the steady flow pattern of $Re = 350$. When we increase the Reynolds number further to 450 and 500, the flow becomes time-dependent and asymmetric with increasing unsteadiness of flow, as shown in Fig. 6e and f. When the flow is unsteady, the jet core is distorted and the main re-circulating vortices emanating from the jet shear layer are alternately shed on both sides of the jet. After the jet impinges on the lower wall, the flow is deflected from the wall and then a wall jet is developed. The wall jet flow is separated from the wall because the flow is disturbed by the wall shear stress, leading to the formation of a series of wall vortices. The detached wall jet flow is partially re-entrained into the jet, which forms a pair of re-circulating zones. Near the jet inlet, small vortices appear between the impinging jet and main re-circulating vortices. These vortices are mainly caused by the existence of the upper wall. The flapping of the jet flow in the unsteady region increases with increasing Reynolds number because of the augmentation of sinuous and varicose

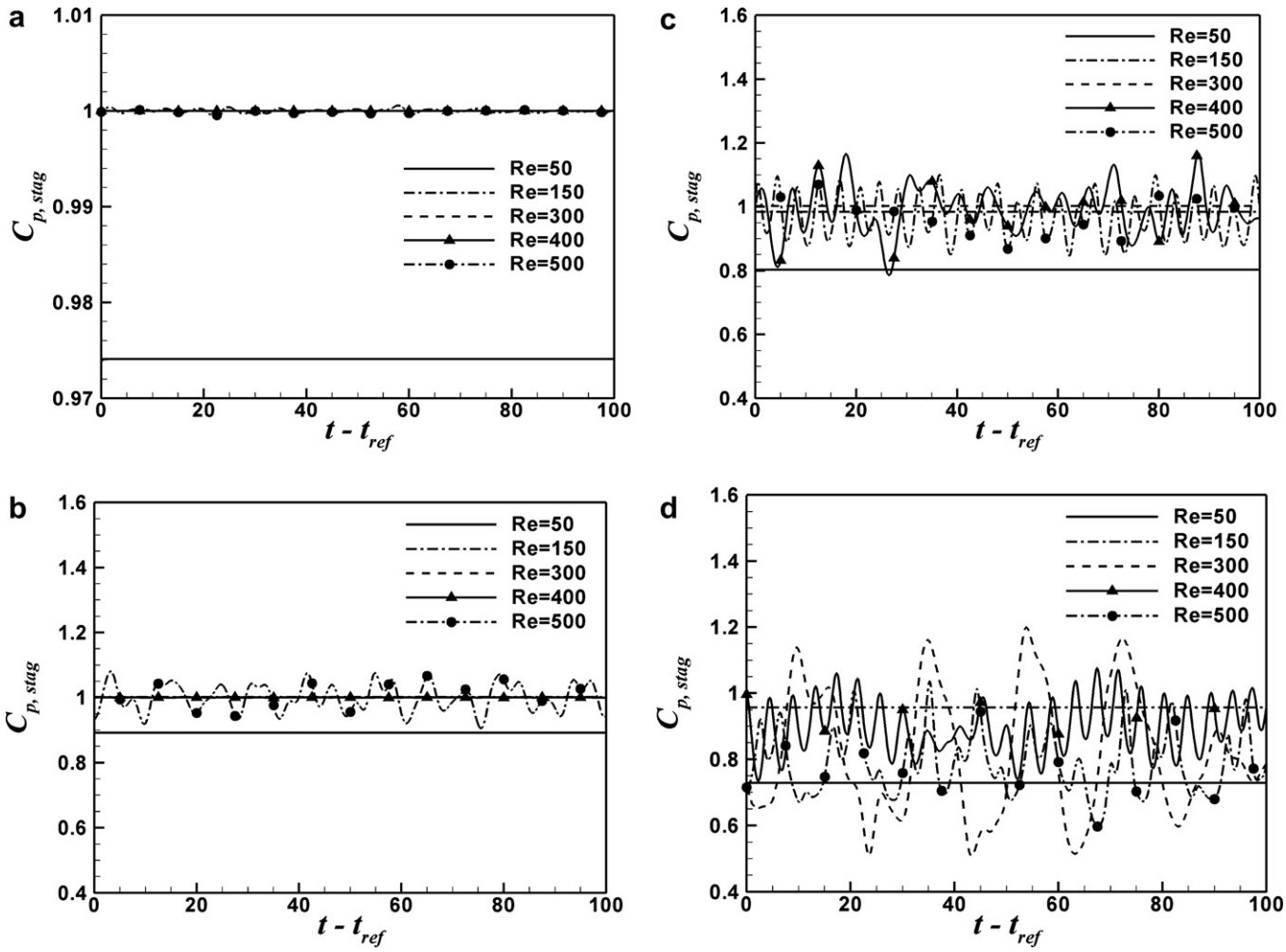

Fig. 4. Time histories of pressure coefficients at the stagnation point ($C_{p,stag}$) for the different height ratios; (a) $H/D = 2$, (b) $H/D = 3$, (c) $H/D = 4$ and (d) $H/D = 5$.

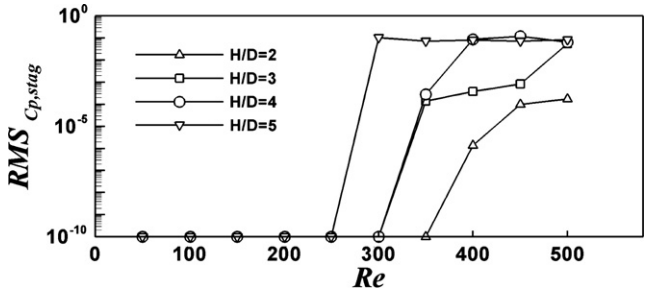

Fig. 5. RMS of pressure coefficient (C_p) at the stagnation point for the different height ratios.

jet instabilities. For the case of $H/D = 2$, even though the flow is time-dependent at the unsteady Reynolds numbers of 400, 450 and 500, the instantaneous jet flow still maintains the almost symmetric pattern near the jet inlet ($x = 0$) because H/D is not large enough to disturb the jet flow near the jet inlet.

For the cases of $H/D = 3$ and 4, the flow is steady and symmetric at $Re \leqslant 300$, which is similar to the case of $H/D = 2$ at $Re \leqslant 350$. When $Re = 150$ for $H/D = 3$ and 4, we can observe the formation of the main re-circulating vortices near the jet inlet and secondary vortices on the lower wall as shown in Figs. 7b and 8b which is similar to the case of $H/D = 2$ at the same Reynolds number. However, the size and strength of the vortices formed at $H/D = 3$ and 4 are larger than those at $H/D = 2$ because the jet entrainment near the jet inlet and the flow instability on the lower wall increase due to increasing domain size with increasing H/D. When $Re = 300$ at $H/D = 3$ and 4, the flow is still steady. However the core of the main re-circulating vortices near the jet inlet is split into two cores and secondary vortices in the lower wall is stretched to the lateral exit along the lower wall. We can also observe the formation of small tertiary vortices in the upper wall surrounded by the main re-circulating vortices. When the Reynolds number is in between 300 and 350, the unsteadiness starts to give some effect on the flow and temperature fields. Thus, when $Re = 350$ at $H/D = 3$ and 4, the flow becomes unsteady and moves toward the lateral exit of the channel with the development of small vortices along

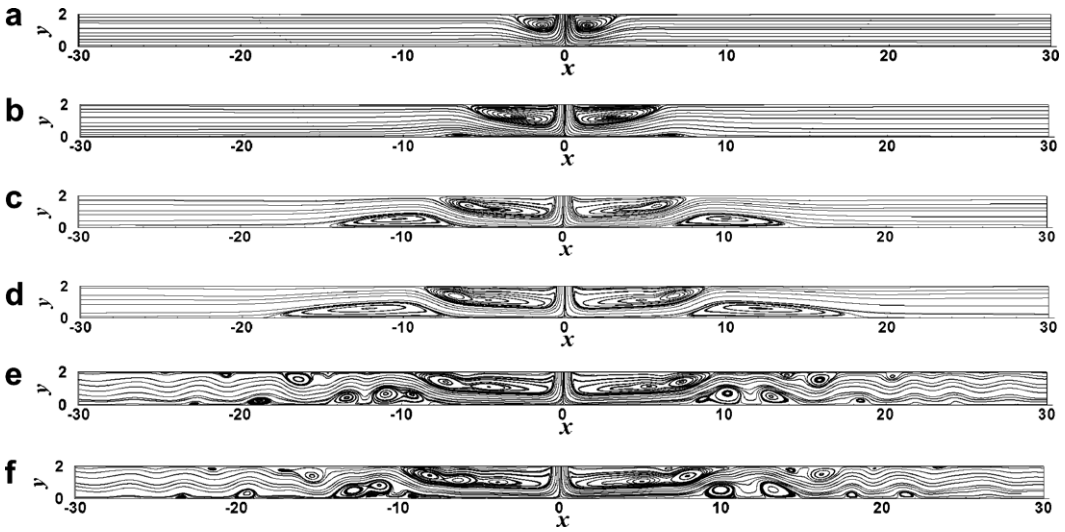

Fig. 6. Instantaneous streamlines at $H/D = 2$ for different Reynolds numbers; (a) $Re = 50$, (b) $Re = 150$, (c) $Re = 300$, (d) $Re = 400$, (e) $Re = 450$ and (f) $Re = 500$.

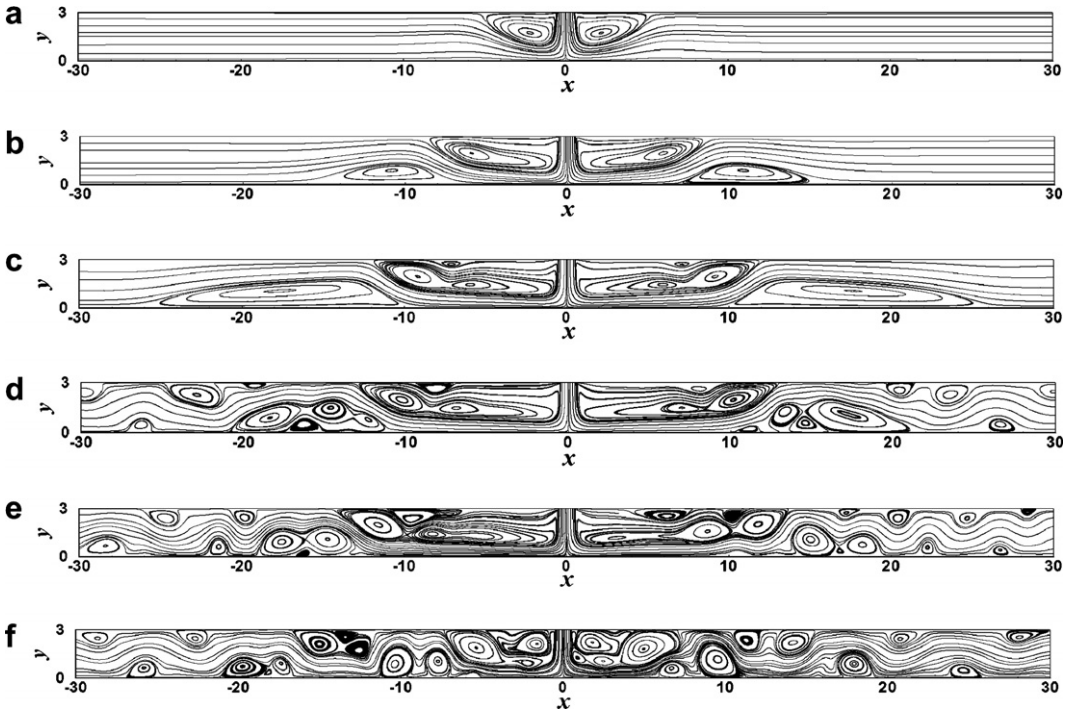

Fig. 7. Instantaneous streamlines at $H/D = 3$ for different Reynolds numbers; (a) $Re = 50$, (b) $Re = 150$, (c) $Re = 300$, (d) $Re = 350$, (e) $Re = 400$ and (f) $Re = 500$.

both the upper and lower walls. If we increase the Reynolds number further to 400 and 500 at $H/D = 3$ and 4, the effect of the unsteadiness on the flow becomes larger and as a result the flows show more complex and irregular patterns as shown in Figs. 7e and f and 8e and f, compared to those at $H/D = 2$ as shown in Fig. 6e and f.

For the case of $H/D = 5$, the jet flow maintains steady and symmetric at $Re = 50$, which is similar to the cases of $H/D = 2$, 3 and 4. However, when $H/D = 5$ at $Re = 50$, the momentum is not large enough to overcome the friction along the lower wall because the domain size and the distance between the jet inlet and the bottom wall increase with increasing H/D. So we can observe the formation of secondary vortices on the lower wall for the case of $H/D = 5$ at $Re = 50$, which is not observed for the cases of $H/D = 2$, 3 and 4. When the Reynolds number increases to 150 at $H/D = 5$, the main re-circulating vortices near the jet inlet are split into two cores and secondary vortices surrounded by the main re-circulating vortices are formed on the upper wall, which are similar to the cases of $H/D = 3$ and 4 at

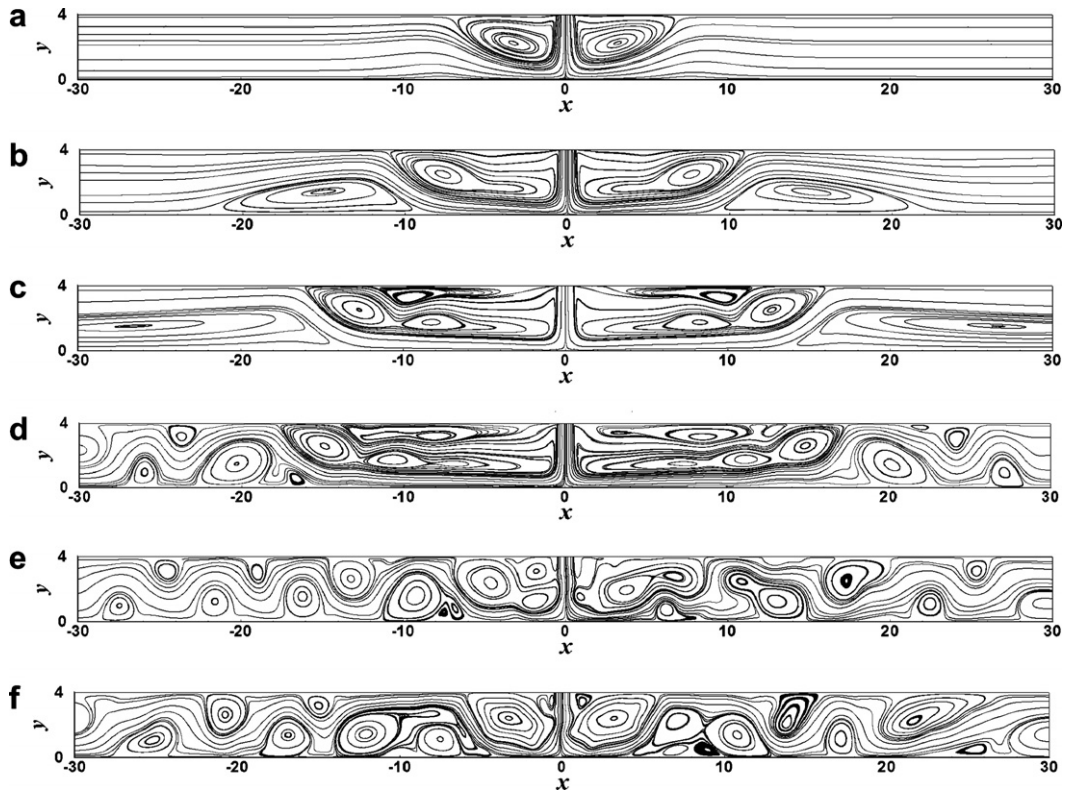

Fig. 8. Instantaneous streamlines at $H/D = 4$ for different Reynolds numbers; (a) $Re = 50$, (b) $Re = 150$, (c) $Re = 300$, (d) $Re = 350$, (e) $Re = 400$ and (f) $Re = 500$.

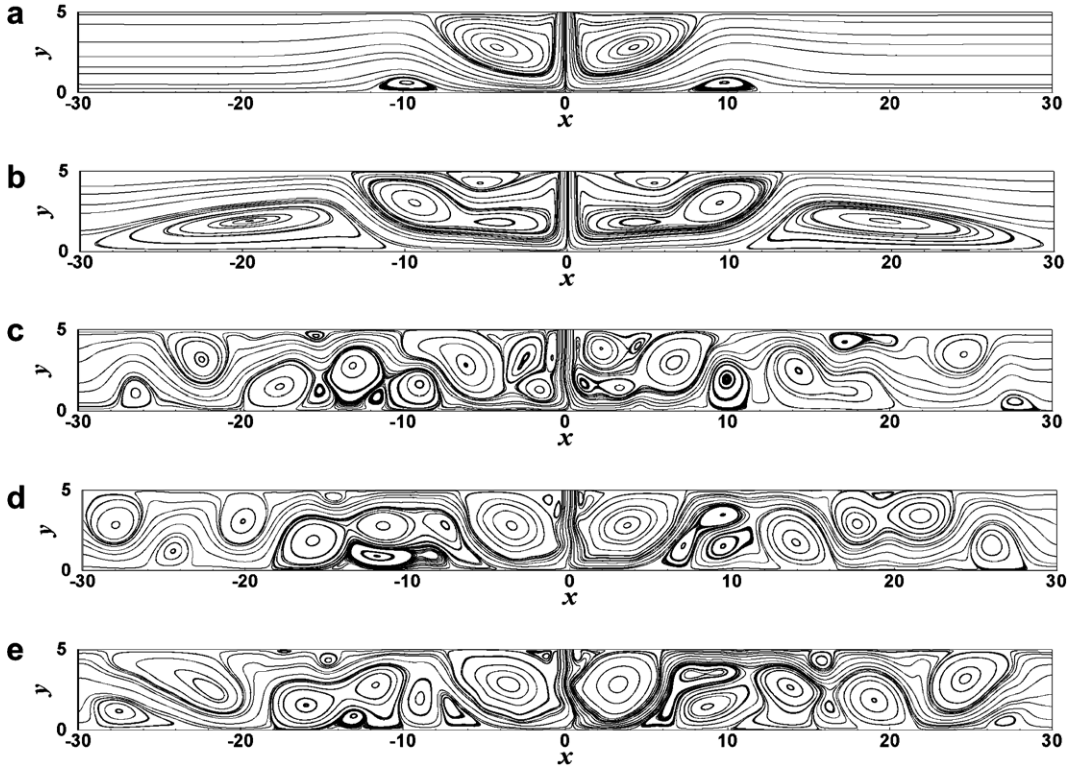

Fig. 9. Instantaneous streamlines at $H/D = 5$ for different Reynolds numbers; (a) $Re = 50$, (b) $Re = 150$, (c) $Re = 300$, (d) $Re = 400$ and (e) $Re = 500$.

$Re = 300$. The size of the secondary vortices formed on the lower wall for the case of $H/D = 5$ is bigger than that for the cases of $H/D = 2$, 3 and 4.

When $Re = 300$, 400 and 500 at $H/D = 5$, the flow becomes unsteady and asymmetric, resulting in complex vortical motion as shown in Fig. 9c–e. When $H/D = 5$, the transition of flow from the steady to unsteady state occurs at a lower Reynolds number than for the cases of $H/D = 2$, 3 and 4 because the unsteadiness increases with increasing H/D. For the case of $H/D = 5$, the instability of the inlet jet gives a much bigger impact on the flow unsteadiness, compared to that for the cases of $H/D = 2$, 3 and 4. Similar to the flow at $Re = 400$ and 500 for the cases of $H/D = 3$ and 4, the time-dependent flow at $Re = 300$, 400 and 500 for the case of $H/D = 5$ shows very complex and irregular patterns in the channel.

Figs. 10–13 show the time-averaged streamlines for the flow fields corresponding to the unsteady region for different Reynolds numbers and H/Ds.

For the case of $H/D = 2$ at the Reynolds numbers of 450 and 500, the time-averaged flow consists of the main re-circulating vortices near the jet inlet (MRV), secondary vortices on the lower wall (LV) and secondary vortices on the upper wall (UV), as shown in Fig. 10. The size of MRV for $Re = 500$ is slightly larger than that for $Re = 450$. However, the size of LV and UV for $Re = 500$ becomes smaller than those for $Re = 450$, due to the increasing convective force with increasing Reynolds number. The center of LV and UV for $Re = 500$ moves more toward the jet axis, compared to that for $Re = 450$.

For the case of $H/D = 3$ at the Reynolds numbers of 350 and 400, the time-averaged flow consists of the main re-circulating vortices near the jet inlet (MRV), small vortices embedded in the main re-circulating flow on the upper wall (UV1) which does not exist for the case of $H/D = 2$, small vortices on the lower wall (LV) and isolated small vortices in the upper wall (UV2), as shown in Fig. 11a and b. When $H/D = 3$, the size of MRV and UV1 for $Re = 400$ is slightly larger than that for $Re = 350$, whereas the size of LV and UV2 for $Re = 400$ becomes smaller and the centers of LV and UV2 move more toward the jet axis, compared to those for $Re = 350$. If we increase the Reynolds numbers to 450 and 500, the UV2 disappears as shown in Fig. 11c and d and the centers of MRV, UV1 and LV keep moving toward the jet axis. As a result, the MRV, UV1 and LV are formed at locations close to the jet axis when $Re = 500$.

For the case of $H/D = 4$ at a Reynolds number of 350, the time-averaged flow consists of the main re-circulating flow near the inlet jet (MRV), small vortices embedded in the main re-circulating vortices on the upper wall (UV1), small vortices in the lower wall (LV1) which does not exist for the case of $H/D = 3$, small vortices embedded in the primary small vortices on the lower wall (LV2) and isolated small vortices on the upper wall (UV2), as shown in Fig. 12a. If we increase the Reynolds numbers to 400 at $H/D = 4$, the LV2 disappears, the size of UV2 becomes bigger, and the size of MRV, UV1 and LV1 becomes smaller, compared to those for $Re = 350$ at $H/D = 4$. The centers of MRV, LV1, UV1 and UV2 move toward the jet axis as the Reynolds number increases from 350 to 400, which is similar to the case of $H/D = 3$, as shown in Fig. 12a and b. The time-averaged flow for $Re = 450$ at $H/D = 4$ is similar to that for $Re = 400$ at $H/D = 4$. If we increase the Reynolds number further to 500 at $H/D = 4$, the flow becomes more complex. The size of MRV and UV1 becomes smaller and the center of MRV and UV1 moves further to the jet axis. The size of LV1 and UV2 becomes larger and LV2 appears again.

The time-averaged flow for the case of $H/D = 5$ at different Reynolds numbers of 300–500 shown in Fig. 13 is similar to that for the case of $H/D = 4$ at $Re = 500$ shown in Fig. 12d, which consists of the MRV, LV1, LV2, UV1 and UV2, because the unsteady effects on the flow increase with increasing H/D. When the Reynolds number increases from 300 to 350 at $H/D = 5$, the size of MRV and UV1 decreases, the center of MRV and UV1 moves toward the jet axis, and the size of LV2 increases. When the Reynolds number is larger than 350 at $H/D = 5$, the time-averaged flow for different Reynolds numbers with the formation of MRV, LV1, LV2, UV1 and UV2 is similar, showing that the time-averaged flow does not depend much on the Reynolds number in the unsteady region at $H/D = 5$.

Fig. 14 shows the time-averaged pressure coefficient at the stagnation point ($\overline{C}_{p,stag}$) as a function of Reynolds number for different height ratios. When $H/D = 2$ and 3, $\overline{C}_{p,stag}$ has a unit value for all Reynolds numbers covering both the steady and unsteady region except $Re = 50$, which means that all the jet momentum at the inlet is transferred into pressure on the impinging wall. When $Re = 50$ at $H/D = 2$ and 3, the value of $\overline{C}_{p,stag}$ is lower than 1 because the convective force of jet flow is not enough to transfer

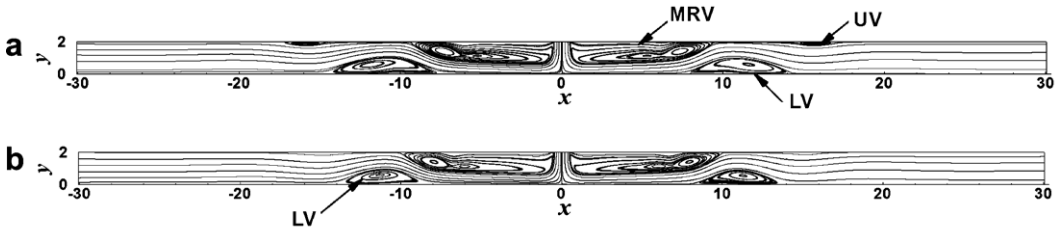

Fig. 10. Time-averaged streamlines at $H/D = 2$ for different Reynolds numbers; (a) $Re = 450$ and (b) $Re = 500$.

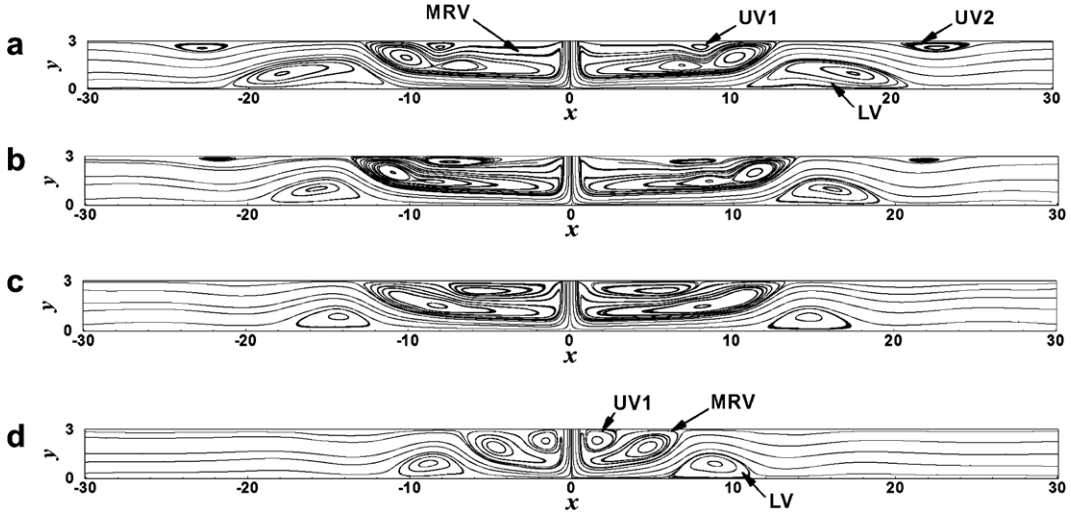

Fig. 11. Time-averaged streamlines at $H/D = 3$ for different Reynolds numbers; (a) $Re = 350$, (b) $Re = 400$, (c) $Re = 450$ and (d) $Re = 500$.

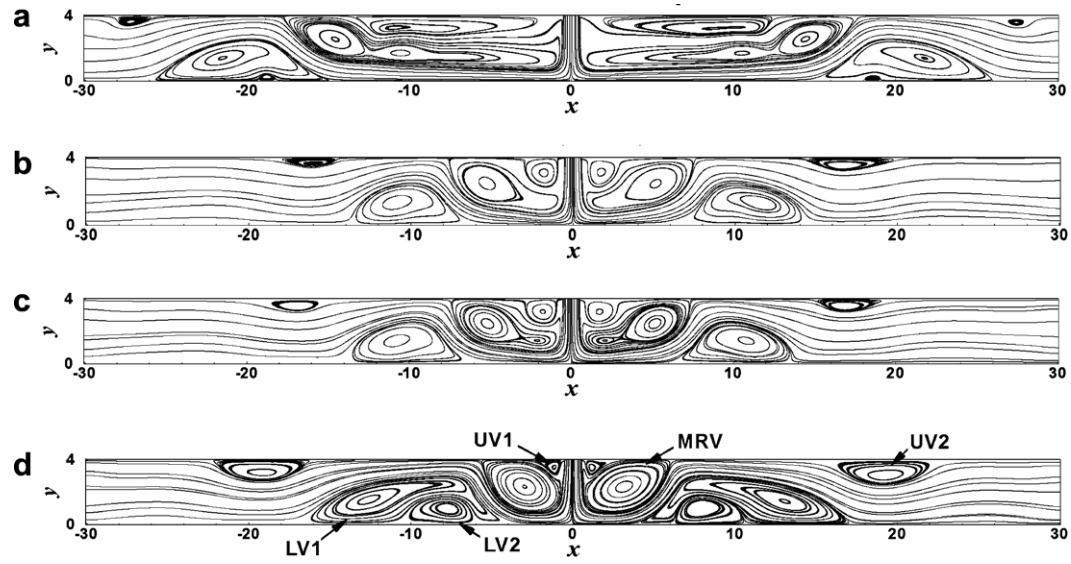

Fig. 12. Time-averaged streamlines at $H/D = 4$ for different Reynolds numbers; (a) $Re = 350$, (b) $Re = 400$, (c) $Re = 450$ and (d) $Re = 500$.

all jet momentum at the inlet into the pressure at the stagnation point at this low Reynolds number. This result also shows the evidence that the jet flow in the unsteady region for the case of $H/D = 2$ and 3 still maintains almost a symmetric shape near the centerline ($x = 0$), as shown in Figs. 6 and 7. If we increase H/D to 4 and 5, the variation of $\overline{C}_{p,stag}$ in the unsteady region is different from that in the steady region. In the steady region at $H/D = 4$ and 5, $\overline{C}_{p,stag}$ has a value less than 1 at $Re = 50$. When we increase the Reynolds number in the steady region at $H/D = 4$ and 5, $\overline{C}_{p,stag}$ increases until it reaches a unit value because the convective force of jet increases with increasing Reynolds number. In the unsteady region at $H/D = 4$ and 5, the jet swings around the centerline due to its flapping motion caused by the unsteadiness. The jet loses its kinetic energy during its flapping motion and dissipates its kinetic energy into the jet induced small vortices. With increasing Reynolds number in the unsteady region at $H/D = 4$ and 5, the unsteadiness and swing motion of jet increases and as a result the jet has less opportunity to impinge on the stagnation point. Thus, if we increase the Reynolds number in the unsteady region at $H/D = 4$ and 5, $\overline{C}_{p,stag}$ decreases continuously with its value less than 1. Because the unsteady effect of $H/D = 5$ is much larger than that of $H/D \leqslant 4$, the values of $\overline{C}_{p,stag}$ for $H/D = 5$ in the unsteady region is much less than that for $H/D \leqslant 4$. In the steady region, $\overline{C}_{p,stag}$ decreases with increasing H/D at the same Reynolds number because the jet flow loses more kinetic energy while it moves the longer distance between the jet inlet and the lower wall with increasing H/D.

Fig. 15 shows the time- and surface-averaged skin friction coefficients ($\overline{\langle C_f \rangle}$) on the lower half wall as a function of Reynolds number for different height ratios. The magnitude of $\overline{\langle C_f \rangle}$ depends on the distance from stagnation point to the 1st separation point, the size and strength of the secondary vortices formed on the lower wall and the location

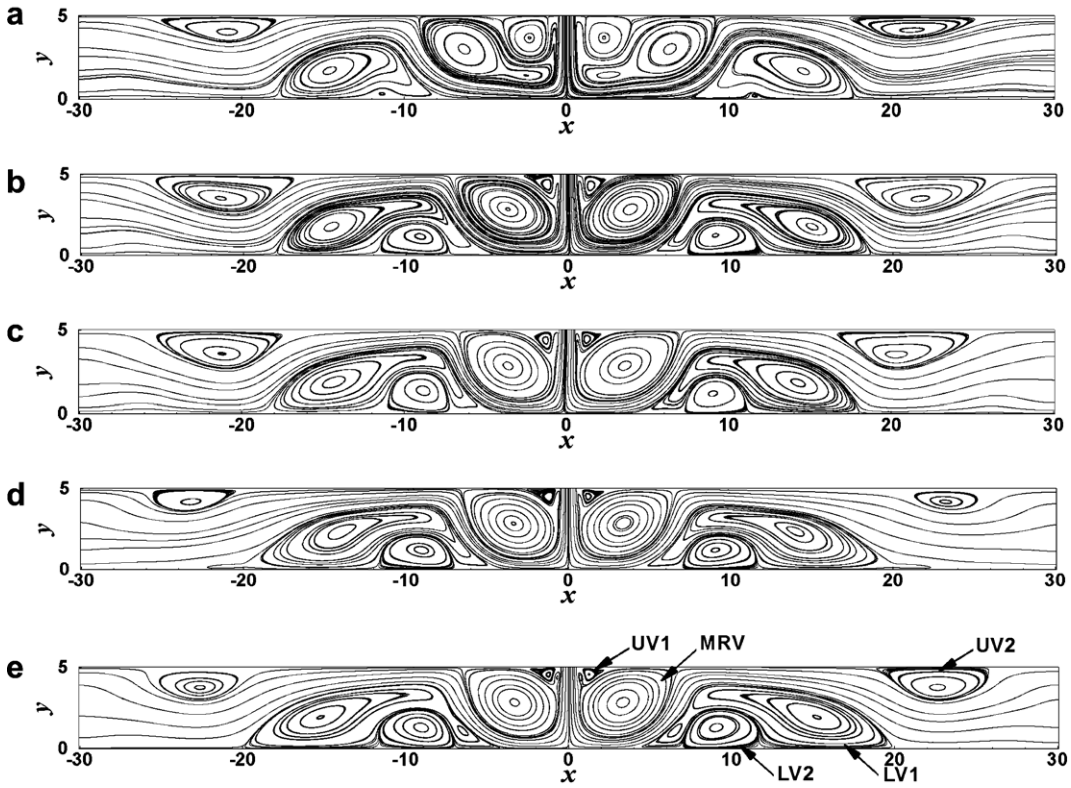

Fig. 13. Time-averaged streamlines at $H/D = 5$ for different Reynolds numbers; (a) $Re = 300$, (b) $Re = 350$, (c) $Re = 400$, (d) $Re = 450$ and (e) $Re = 500$.

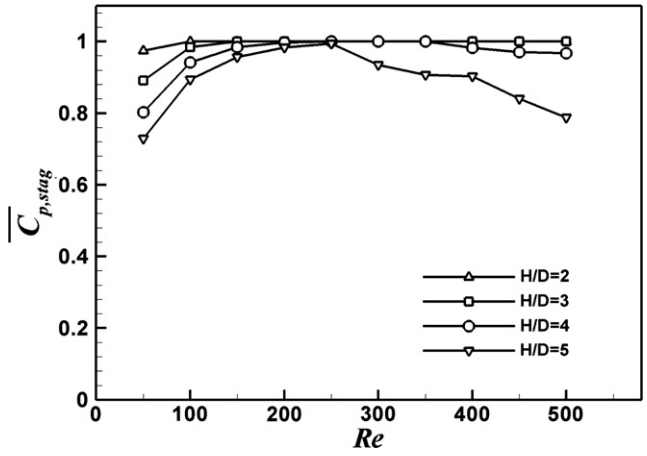

Fig. 14. Time-averaged pressure coefficient at stagnation point ($\overline{C}_{p,stag}$) as a function of Reynolds number for different height ratios.

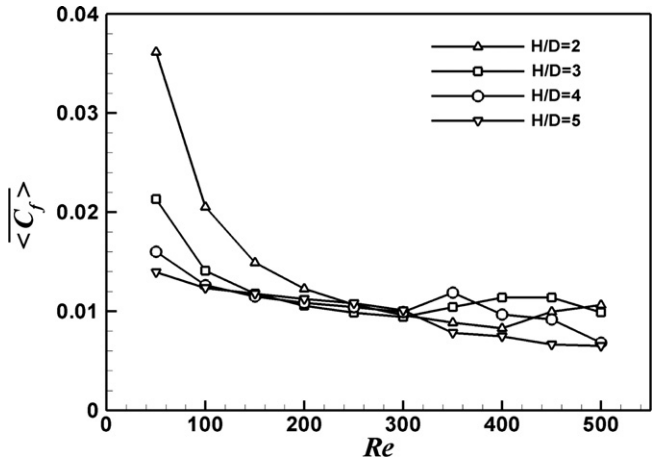

Fig. 15. Time- and surface-averaged skin friction coefficients ($\overline{\langle C_f \rangle}$) on the impingement wall as a function of Reynolds number for different height ratios.

of the reattachment point, whose respective effects a give positive or negative effect on $\overline{\langle C_f \rangle}$. As the Reynolds number increases in the steady flow region, the 1st separation point on the lower wall is located at a longer distance from the centerline and the size of secondary vortices formed on the lower wall increases. As a result, $\overline{\langle C_f \rangle}$ in the steady flow region decreases with increasing Reynolds number. However, in the unsteady flow region, the variation of $\overline{\langle C_f \rangle}$ does not depend much on the Reynolds number and H/D unlike to the large variation of $\overline{\langle C_f \rangle}$ in the steady flow region.

Fig. 16 shows the time-averaged Nusselt number at the stagnation point, $\overline{Nu}_{stag}$, as a function of Reynolds number for different height ratios. The time-averaged Nusselt number in Fig. 16 is divided by $Pr^{1/3}$. For a fixed H/D, $\overline{Nu}_{stag}$ increases with increasing Reynolds number generally because the convective heat transfer increases with increasing Reynolds number. As we increase H/D for the fixed Reynolds number, the cold jet flow travels a longer distance until it meets the lower hot wall. And as a result the thermal boundary layer around the stagnation point

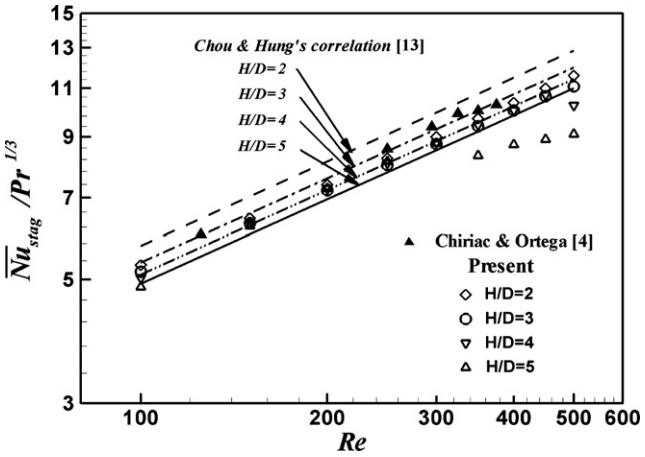

Fig. 16. Time-averaged Nusselt number at the stagnation point as a function of Reynolds number for the different height ratios.

becomes thicker. Thus, $\overline{Nu}_{stag}$ decreases with increasing H/D for a fixed Reynolds number. We compared our computational results of $\overline{Nu}_{stag}$ with the correlation obtained by Chou and Hung [13] and the computational results for $H/D = 5$ obtained by Chiriac and Ortega [4]. In the steady region, the variation of $\overline{Nu}_{stag}$ obtained by the present computation for different values of H/D is slightly smaller than that of the correlation of Chou and Hung [13] and the present computational results of $\overline{Nu}_{stag}$ for $H/D = 5$ at $Re = 125$ and 250 is slightly lower than $\overline{Nu}_{stag}$ obtained by Chiriac and Ortega [4]. In general, our computational results for $\overline{Nu}_{stag}$ in the steady region represent the results given by Chiriac and Ortega [4] and Chou and Hung's correlation [13] well. However, in the unsteady region, our computational results are much lower than those obtained by Chou and Hung's correlation because of the swing motion caused by the unsteadiness. We can also observe the similar drop in the value of $\overline{Nu}_{stag}$ obtained by Chiriac and Ortega [4] in the unsteady region. Chou and Hung [13] solved the two-dimensional, steady governing equations of mass, momentum and energy conservation with a Reynolds number range of 100–500, even though these Reynolds numbers cover the unsteady region. So Chou and Hung's correlation [13] cannot reproduce the effects of unsteadiness on $\overline{Nu}_{stag}$ and as a result we can observe big differences between our computational results and Chou and Hung's correlation [13] for $\overline{Nu}_{stag}$ in the unsteady region.

Fig. 17 shows the distributions of time-averaged Nusselt numbers ($\overline{Nu}$) normalized by $Re^{1/2}$ along the lower wall for

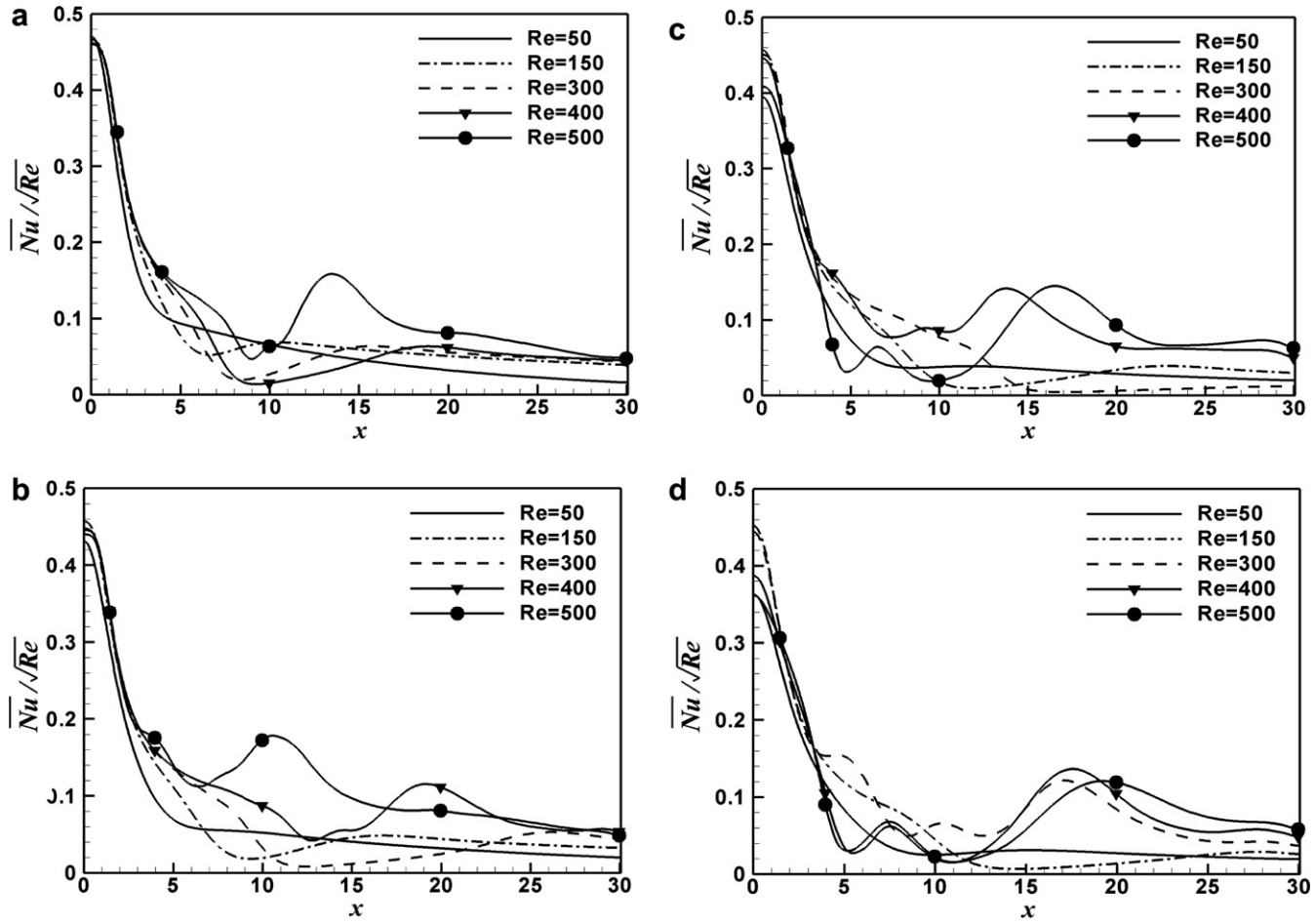

Fig. 17. Time-averaged Nusselt number at the impingement wall for the different height ratios.; (a) $H/D = 2$, (b) $H/D = 3$, (c) $H/D = 4$, (d) $H/D = 5$.

different Reynolds numbers and height ratios. Only a half of the lower wall is considered in the plot because the time-averaged quantities are symmetric about the jet axis ($x = 0$). The distribution of $\overline{Nu}/\sqrt{Re}$ along the lower wall generally follows the Reynolds analogy [8] and depends strongly on the size and magnitude of the secondary vortices formed on the lower wall. $\overline{Nu}/\sqrt{Re}$ has a peak value at the stagnation point. For the case without secondary vortices on the lower wall, $\overline{Nu}/\sqrt{Re}$ decreases very rapidly close to the stagnation point and then keeps decreasing slowly as the flow approaches to the lateral exit. However, for the case with secondary vortices, $\overline{Nu}/\sqrt{Re}$ increases slightly between the separation and reattachment point in the presence of secondary vortices.

5. Conclusions

The present study investigates numerically the unsteady two-dimensional fluid flow and heat transfer in the confined impinging slot jet for different Reynolds numbers of 50–500 and different height ratios of 2–5. The critical Reynolds number, beyond which the flow and temperature fields start to change their state from steady to unsteady, depends on the height ratio.

If the Reynolds number is greater than the critical Reynolds number, the flow and thermal fields becomes time-dependent and asymmetric. As the Reynolds number increases in the unsteady region, the flapping motion of jet increases and the flow fields become more complex with unsteady vortical motion caused by the augmentation of sinuous and varicose jet instability.

When $H/D = 2$ and 3, the time-averaged pressure coefficient at the stagnation point ($\overline{C}_{p,stag}$) has a unit value for all Reynolds numbers covering both the steady and unsteady region except $Re = 50$. When $H/D = 4$ and 5, $\overline{C}_{p,stag}$ in the steady region increases from a value lower than 1 to the unity value, whereas $\overline{C}_{p,stag}$ in the unsteady region decreases with increasing flapping motion of the jet caused by the unsteadiness, if we increase the Reynolds number in the steady and unsteady regions.

In the steady region, the time- and surface-averaged skin friction coefficients ($\overline{\langle C_f \rangle}$) decrease with increasing Reynolds number and decrease with increasing height ratios. However, the dependency of $\overline{\langle C_f \rangle}$ on the Reynolds number and height ratio in the unsteady region is not large.

In the steady region, the time-averaged Nusselt number at the stagnation point ($\overline{Nu}_{stag}$) increases monotonically with increasing Re for different height ratios. However, $\overline{Nu}_{stag}$ in the unsteady region decreases due to the increasing flapping motion of the jet with increasing Reynolds number.

The distribution of time-averaged Nusselt numbers ($\overline{Nu}$) along the lower wall depends strongly on the size and magnitude of the secondary vortices formed on the lower wall. $\overline{Nu}$ has the maximum value at the stagnation point and decreases generally as we move to the lateral exit, except the locations where $\overline{Nu}$ increases slightly in the presence of secondary vortices.

Acknowledgements

This work was supported by the Korea Foundation for International Cooperation of Science & Technology (KICOS) through a grant provided by the Korean Ministry of Science & Technology (MOST) in 2007(2008) (No. K20702000013-07E0200-01310).

References

[1] E.M. Sparrow, T.C. Wong, Impingement transfer coefficients due to initially laminar slot jets, Int. J. Heat Mass Transfer 18 (1975) 597–605.
[2] M. Chen, R. Chalupa, A.C. West, V. Modi, High Schmidt mass transfer in a laminar impinging slot jet flow, Int. J. Heat Mass Transfer 43 (2000) 3907–3915.
[3] L.B.Y. Aldabbagh, I. Sezai, Numerical simulation of three-dimensional laminar multiple impinging square jets, Int. J. Heat Fluid Flow 23 (2002) 509–518.
[4] V.C. Chiriac, A. Ortega, A numerical study of the unsteady flow and heat transfer in a transitional confined slot jet impinging on an isothermal surface, Int. J. Heat Mass Transfer 45 (2002) 1237–1248.
[5] H.G. Lee, M.Y. Ha, H.S. Yoon, A numerical study on the fluid flow and heat transfer in the confined jet flow in the presence of magnetic field, Int. J. Heat Mass Transfer 48 (2005) 5297–5309.
[6] F.C. Hsieh, J.H. Wu, J.C. Hsieh, T.F. Lin, Unstable vortex flow and new inertia-driven vortex rolls resulting from air jet impinging onto a confined heated horizontal disk, Int. J. Heat Mass Transfer 49 (2006) 4697–4711.
[7] D.J. Phares, G.T. Smedley, R.C. Flagan, The wall shear stress produced by the normal impingement of a jet on a flat surface, J. Fluid Mech. 418 (2000) 351–375.
[8] Y.M. Chung, K.H. Luo, N.D. Sandham, Numerical study of momentum and heat transfer in unsteady impinging jets, Int. J. Heat Fluid Flow 23 (2002) 592–600.
[9] H.S. Law, J.H. Masliyah, Numerical prediction of the flow field due to a confined laminar two-dimensional submerged jet, Comput. Fluids 12 (1984) 199–215.
[10] D.M. Schafer, S. Ramadhyani, F.P. Incropera, Numerical simulation of laminar convection heat transfer from an in-line array of discrete sources to a confined rectangular jet, Numer. Heat Transfer A (1992) 121–141.
[11] H. Miyazaki, E. Silberman, Flow and heat transfer on a flat plate normal to a two-dimensional laminar jet issuing from a nozzle of finite height, Int. J. Heat Mass Transfer 15 (1972) 2097–2107.
[12] D. Sahoo, M.A.R. Sharif, Numerical modeling of slot-jet impingement cooling of a constant heat flux surface confined by a parallel wall, Int. J. Therm. Sci. 43 (2004) 877–887.
[13] Y.J. Chou, Y.H. Hung, Impingement cooling of an isothermally heated surface with a confined slot jet, ASME J. Heat Transfer 116 (1994) 479–482.
[14] A. Chatterjee, L.J. Deviprasath, Heat transfer in confined laminar axisymmetric impinging jets at small nozzle-plate distances: the role of upstream vorticity diffusion, Numer. Heat Transfer Part A (2001) 777–800.
[15] Z.H. Lin, Y.J. Chou, Y.H. Hung, Heat transfer behaviors of a confined slot jet impingement, Int. J. Heat Mass Transfer (1997) 1095–1107.
[16] A.R.P. van Heiningen, A.S. Mujumdar, W.J.M. Douglas, Numerical prediction of the flow field and impingement heat transfer caused by a laminar slot jet, J. Heat Transfer Trans. ASME (1976) 654–658.
[17] Y. Zang, R.L. Street, J.R. Koseff, A non-staggered grid, fractional step method for time-dependent incompressible Navier–Stokes equations in curvilinear coordinate, J. Comput. Phys. 114 (1994) 18–33.

[18] J. Kim, P. Moin, Application of a fractional-step method to incompressible Navier–Stokes equations, J. Comp. Phys. 59 (1985) 308–323.
[19] S. Satake, T. Kunugi, Direct numerical simulation of an impinging jet into parallel disks, Int. J. Numer. Meth. Heat Fluid Flow 8 (1998) 768–780.
[20] L.R. Pauley, P. Moin, W.C. Reynolds, The structure of two-dimensional separation, J. Fluid Mech. 220 (1990) 397–411.
[21] P.S. Pacheco, Parallel Programming with MPI, Morgan kaufmann Publishers Inc, 1997.